

Ambient plasma synthesis of TiO₂@graphite oxide nanocomposites for efficient photocatalytic hydrogenation†

Jeong Hoon Byeon^{*a} and Jang-Woo Kim^{*b}Cite this: *J. Mater. Chem. A*, 2014, 2, 6939Received 17th January 2014
Accepted 21st February 2014

DOI: 10.1039/c4ta00287c

www.rsc.org/MaterialsA

A graphite oxide (GO) layer with ordered ultrafine TiO₂ particles was synthesized using an ambient heterogeneous spark and the resulting materials displayed enhanced photocatalytic activity for hydrogen production. The ability of the TiO₂@GO nanocomposites to produce hydrogen was significantly greater than that of spark-produced TiO₂ particles, and even of p25-TiO₂ and p25-TiO₂@large reduced graphene oxide (LrGO). Even though nanoscale rGO hybridization with TiO₂ nanoparticles resulted in the highest performance in hydrogenation, this ambient plasma synthesis of TiO₂@GO composites nevertheless did make an appropriate structure for the photocatalytic performance comparable to that of p25-TiO₂@LrGO without individual chemical preparation of rGO.

Introduction

Photocatalytic technology could supply a feasible way to alleviate energy and environmental problems through splitting water for hydrogen production and degrading toxic pollutants.^{1,2} Semiconductor photocatalysis, one of the most promising technologies, is mainly applied to clean hydrogen energy production and environmental remediation applications.³ Titanium oxide (TiO₂), due to its cheapness, nontoxicity, effectiveness, and photostability, is becoming more popular for use with various semiconductor materials.⁴ Unfortunately, because of its large band gap of 3.2 eV, it can utilize only a very small UV fraction (~4%) of available solar light; hence, it has aroused great interest for extending the photoresponse of TiO₂ to the visible light region for better solar light utilization. Another major limitation for achieving high photocatalytic activity is the rapid recombination of charge carriers. The charge pair recombination, which is faster than the interfacial charge transfer, reduces the quantum efficiency of photocatalysis.⁵

Numerous efforts have been made in the last few decades to improve the photocatalytic activity of semiconductor photocatalysts. Aside from tuning their nanostructure and chemical composition, hybrid catalysts prepared by immobilization of the photoactive nanoparticles on appropriate substrates have been explored because of the significantly improved performance observed on such composites,^{6–8} among them, the

potential role of carbon materials as additives and supports (*i.e.* conjugated carbon materials) for the immobilization of photocatalyst nanoparticles has recently attracted considerable attention^{9–13} because of the high efficiencies reported for carbon-photocatalyst composites on the photodegradation of a variety of pollutants in both the liquid and the gas phase.^{14–16}

Conjugated carbon materials such as carbon nanotubes, fullerenes, graphene, and graphite are excellent candidates for improving the transport of photocarriers during photocatalysis through the formation of electronic interactions with photocatalyst nanoparticles.¹⁷ Among them, carbon nanotubes, fullerenes, and graphenes are more expensive than graphite because they require complex manufacturing processes.⁴ Graphite oxide (GO) is a member of conjugated carbon materials that have a lamellar structure and has attracted great interest among researchers owing to some of its potential applications for electrochemical devices, catalysis, energy storage, and adsorption, and furthermore, GO is the most readily available, inexpensive, and suitable for mass production.¹⁸ However, GO produced through a harsh oxidation treatment of graphite sheets is usually used as the starting material in most studies.¹⁹ Moreover, its hybridization with photocatalyst nanoparticles requires additional batch chemical steps and control of the preparation of the nanoparticles,²⁰ and thus it is still a challenge to prepare the hybrid photocatalysts in a lesser waste and continuous synthesis manner.

The present work introduces an ambient heterogeneous spark discharge to assemble TiO₂@GO nanocomposites for enhancement of photocatalytic hydrogen production. In our previous work, we reported the creation of different carbonaceous nanostructures by controlling the conditions of heterogeneous spark discharges.²¹ This is the first attempt to synthesise *in situ* oxidized metal-carbon nanostructures in a

^aDepartment of Chemistry, Purdue University, Indiana 47907, USA. E-mail: jbyeon@purdue.edu; Tel: +1 765 494 5499

^bDepartment of Digital Display Engineering, Hoseo University, Asan 336-795, Republic of Korea. E-mail: jwkim@hoseo.edu; Tel: +82 41 540 5925

† Electronic supplementary information (ESI) available. See DOI: 10.1039/c4ta00287c

continuous gas-phase manner without using any wet chemical steps under ambient conditions. A graphite–titanium spark configuration in an $\text{N}_2\text{--CO}_2\text{--O}_2$ atmosphere was employed to produce $\text{TiO}_2\text{@GO}$ nanocomposites, and the nanocomposites were separated using mechanical filtration. Finally, they were employed as photocatalysts to produce hydrogen. The as-formed $\text{TiO}_2\text{@GO}$ nanocomposites exhibited significantly higher photocatalytic activity than that from commercial and spark-produced TiO_2 nanoparticles. The mechanism of enhanced photocatalytic activity is based on the high migration efficiency of photoinduced electrons at the $\text{TiO}_2\text{--GO}$ interface, which is due to the electronic interaction between both materials. We also evaluated the photocatalytic stability of the nanocomposites by repeating the experiment five times for stronger confirmation.

Results and discussion

The gas temperature inside the spark channel was increased beyond a critical value of 4000 K, which was sufficient to sublimate parts of the titanium and graphite electrodes.²² The duration of each spark was very short and the vapors cooled rapidly downstream of the spark. This formed a supersaturation resulting in particle formation through nucleation–condensation. The total number concentration (TNC), geometric mean diameter (GMD), and geometric standard deviation (GSD) of the TiO_2 particles, which were measured using a scanning mobility particle sizer (SMPS, 3936, TSI, US), were 9.04×10^6 particles cm^{-3} , 22.7 nm, and 1.63, respectively, as shown in Fig. 1. $\text{TiO}_2\text{@GO}$ nanocomposites were formed near the spark channel by incorporating titanium with graphite under an oxygen existing environment. We verified the incorporation of TiO_2 particles with GO layers by measuring the size distributions of GO and $\text{TiO}_2\text{@GO}$ in the gas-phase. Table S1† summarizes the size distribution measurements of GO and $\text{TiO}_2\text{@GO}$. The TNC, GMD, and GSD of the $\text{TiO}_2\text{@GO}$ case were 7.61×10^6 particles

cm^{-3} , 19.6 nm and 1.63, respectively. The analogous data for GO were 4.84×10^3 cm^{-3} , 73.8 nm, and 2.92, respectively. The size distribution of $\text{TiO}_2\text{@GO}$ was rather similar to that of TiO_2 particles compared to that of GO, and there was no bimodal distribution character, implying that GO was nearly quantitatively incorporated with TiO_2 , to form $\text{TiO}_2\text{@GO}$ nanocomposites.

Low- and high-magnification transmission electron microscopy (TEM, JEM-3010, JEOL, Japan) images (Fig. 2) show the morphology of TiO_2 and $\text{TiO}_2\text{@GO}$ samples. Specimens were prepared for examination using TEM by direct electrostatic gas-phase sampling at a sampling flow rate of 1.0 L min^{-1} and an operating voltage of 5 kV using a Nano Particle Collector (NPC-10, HCT, Korea). The TEM images reveal that the TiO_2 particles were agglomerates (~ 20 nm in lateral dimension) of several primary particles, which is consistent with the SMPS data (measured agglomerated TiO_2 particles) noted in Table S1.† As shown in the inset of TiO_2 , about 0.35 nm size of the lattice fringe of TiO_2 can be observed, which can be indexed to the (101) plane of the tetragonal structure. The crystalline structure of TiO_2 was further analyzed using X-ray diffraction (Fig. S1a†). When the heterogeneous spark discharge was employed, most TiO_2 particles were attached to the GO layers, resulting in $\text{TiO}_2\text{@GO}$ nanocomposites. It seems that the co-condensation of the vapors resulted in carbon incorporation with TiO_2 particles during the spark process. The production yield of $\text{TiO}_2\text{@GO}$ nanocomposites from the ambient plasma synthesis is approximately 83.4%. The yield was determined by the area fraction of $\text{TiO}_2\text{@GO}$ -to-all particles in the TEM image. The TEM image shows the larger sizes of the nanocomposites owing to gathering individual nanocomposites during the direct electrostatic gas-phase sampling. Nevertheless, the GO layers were clearly seen and had a d -spacing of about 0.44 nm (see the inset).²³ The increased basal spacing of GO (vs. a graphite

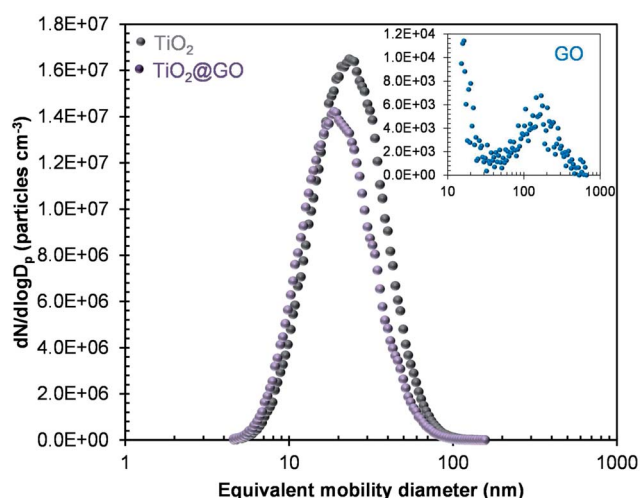


Fig. 1 Size distributions of spark-produced individual TiO_2 and GO particles and their incorporated nanostructures ($\text{TiO}_2\text{@GO}$) in the gas-phase. Standard deviations are noted in Table S1.†

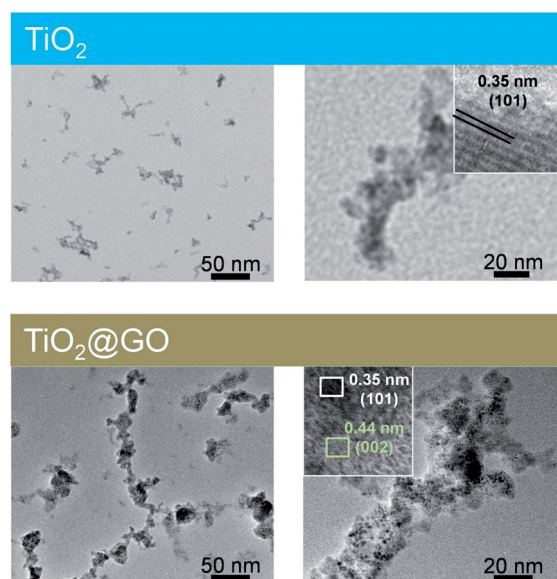


Fig. 2 Low- and high-magnification TEM images of TiO_2 (20 ± 4.4 nm) and $\text{TiO}_2\text{@GO}$ (26 ± 8.6 nm) samples.

interspacing of 0.34 nm) is related to the accommodation of various oxygen species and to the changes in the carbon hexahedron grid plane, indicating that the graphite was efficiently oxidized. While the boundary of TiO_2 particles within the nanocomposites was a little bit ambiguous probably due to agglomeration between TiO_2 and GO particles.

Fig. 3a gives the photoelectricity results of the TiO_2 and $\text{TiO}_2@\text{GO}$ samples using a photocurrent test with a cutoff filter. The potential of the working electrode against the Pt counter electrode is set at 0.0 V. It was observed that there was a fast and uniform photocurrent response to each turn-on and off event in both electrodes. TiO_2 showed a maximum photocurrent in the UV range that is located at ~ 330 nm, while no significant photocurrent was generated under visible irradiation. Interestingly, $\text{TiO}_2@\text{GO}$ showed a broad but much more intense photocurrent peak covering the range to 450 nm, thus extending into the visible range. Its maximum signal appeared at ~ 350 nm, 20 nm red-shifted from that of TiO_2 . The photocurrent density of the TiO_2 and $\text{TiO}_2@\text{GO}$ samples was 0.02 and 0.11 mA cm^{-2} (0.83 and 4.14×10^{-4} A in photocurrent, inset) at 350 nm wavelength, respectively. The current of TiO_2 was enhanced more than five times by incorporation with GO. The high photocurrents measured in the nanocomposites are related to a higher density of photogenerated electrons recovered at the back contact of the electrical circuit likely as a result of efficient charge carrier separation; this indicates that the incorporation of GO plays an important role in the photoelectrochemical response of the nanocomposites, and anticipates a potentially higher photocatalytic activity of the nanocomposites. The time profiles of hydrogen production are compared among samples in Fig. 3b. Compared with p25- TiO_2 , TiO_2 , and GO, $\text{TiO}_2@\text{GO}$ enhanced the hydrogen production performance. p25- TiO_2 had a size of 32.4 nm, a specific surface area of 52 $\text{m}^2 \text{g}^{-1}$, and an anatase : rutile ratio of 82 : 18. The specific surface areas of TiO_2 , GO, and $\text{TiO}_2@\text{GO}$ are 126.4,

100.8, and 225.2 $\text{m}^2 \text{g}^{-1}$, respectively. Incorporation between TiO_2 and GO was the most suitable to form void areas due to a significant difference in the morphology. The p25- TiO_2 shows a slightly larger hydrogen production than the spark produced TiO_2 particles, and this might have originated from the difference in the anatase : rutile ratio (69 : 31 for spark produced TiO_2). The hybridization assisted the photocatalysis by withdrawing electrons and subsequently retarding the charge pair recombination. Previous studies have also explained that the enhanced photocatalytic activity of the $\text{TiO}_2@\text{GO}$ hybrid materials is mainly attributed to the inhibition of charge recombination.⁴ In the present case, the incorporation of GO with ultrafine TiO_2 particles did make an appropriate structure for enhanced photocatalytic performance. Therefore, the photo-generated conduction band electrons in TiO_2 could be more easily transferred to GO layers, because there is good contact between the TiO_2 surface and the GO layer. Further, even after five cycles (inset of Fig. 3b), we found that the hydrogen production performance reduced only by *ca.* 8% from 44.7 to 40.8 $\mu\text{mol h}^{-1}$, suggesting that the nanocomposites have good stability and reusability. The quantum yield (QY) of the photocatalytic production of hydrogen [$\text{QY}(\%) = (2 \times R/I) \times 100$, where R and I are the hydrogen production rate and coefficient (Einstein s^{-1})] at 420 nm in wavelength was approximately 9.3%. The presence of GO on the surface of TiO_2 could inhibit the photocorrosion phenomenon and enhance the stability of the TiO_2 photocatalyst greatly. On the other hand, the slight decrease in the performance among the cycles is probably attributed to the aggregation of TiO_2 particles on the GO layers after several runs, which results in the decrease in surface area, and finally leads to the decrease in photocatalytic activity. In addition, about 85% of carbon was produced when the polarity of spark electrodes was switched as Ti:cathode-C:anode, and the hydrogen production was significantly smaller ($\sim 7.4 \mu\text{mol h}^{-1}$) than that from the present work. A further

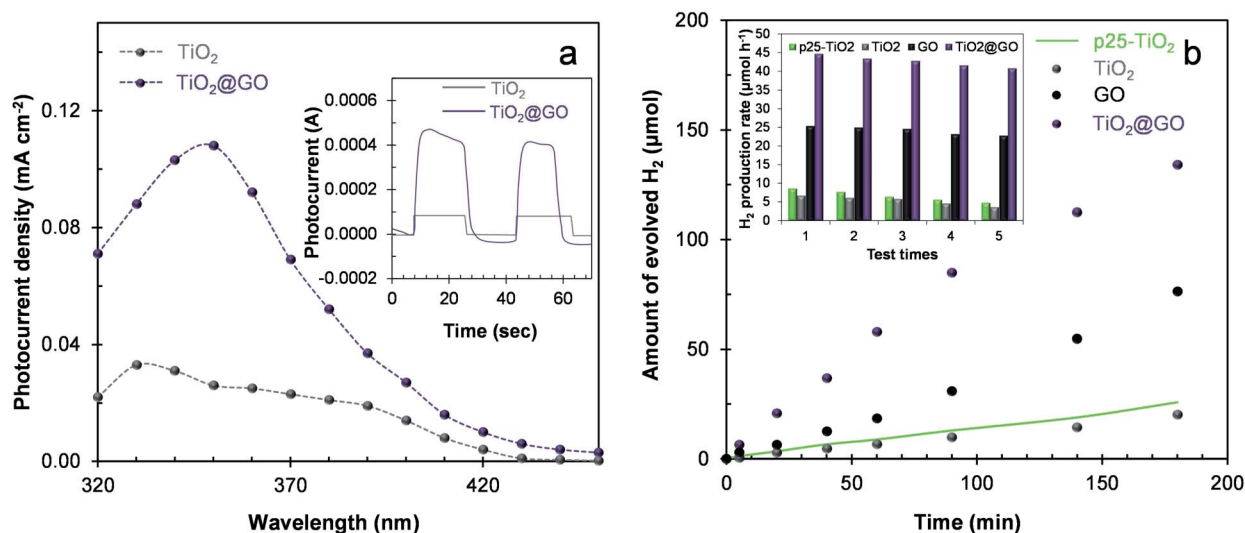


Fig. 3 Photocatalytic performances of $\text{TiO}_2@\text{GO}$ nanocomposites for hydrogen production. (a) Photoelectrochemical responses of TiO_2 and $\text{TiO}_2@\text{GO}$ samples with different light wavelengths (and on-off configuration, inset). (b) Time profiles of hydrogen production with p25- TiO_2 , spark-produced TiO_2 , GO, and $\text{TiO}_2@\text{GO}$ samples. Repeated runs of hydrogen production are also displayed (inset).

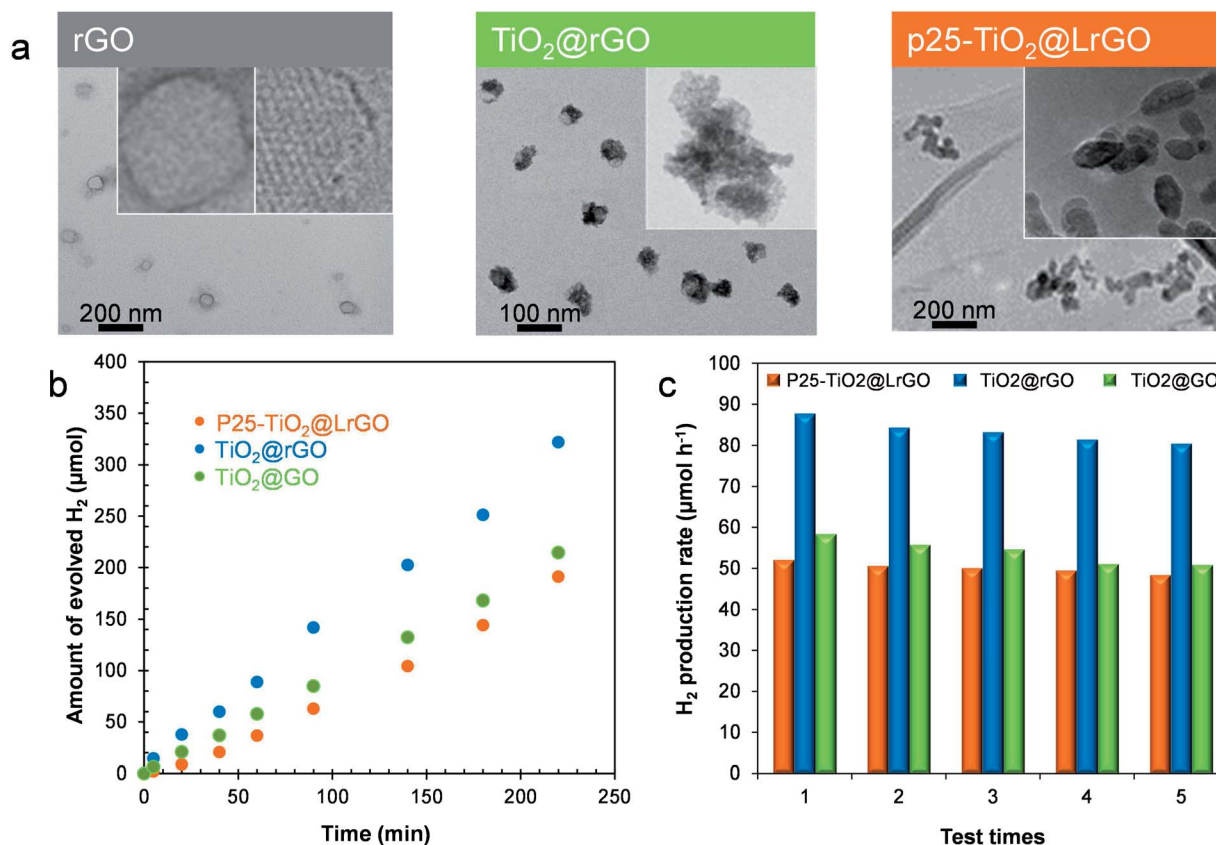


Fig. 4 Comparison of hydrogenation performance of rGO hybridized composites. (a) Low- and high-magnification TEM images of rGO, TiO₂@rGO, and p25-TiO₂@LrGO samples. (b) Time profiles of hydrogen production with p25-TiO₂@LrGO, TiO₂@rGO and TiO₂@GO composites. (c) Repeated runs of hydrogen production.

study for precisely controlling the ratio between TiO₂ and GO for the most efficient hydrogen production *via* ambient spark discharge is in progress.

In order to evaluate the feasibility of the synthesized TiO₂@GO, hydrogenation performances between the present composites and the TiO₂@reduced graphene oxide (rGO, MKN-SLG-F, M K Impex Corp., Canada) were tested. Hence, we further prepared different setups for fabricating TiO₂@rGO and p25-TiO₂@large rGO (LrGO, G250, Sinocarbon, China) composites. According to a previous study,⁹ the size of TiO₂@graphene is one of the critical parameters for efficient hydrogen production, and thus we employed TiO₂@rGO and p25-TiO₂@LrGO as representative comparators. In the case of TiO₂@rGO, we employed the BR method²⁴ to fabricate nanoscale TiO₂@rGO composites since there are better contacts between the TiO₂ surface and rGO flakes.⁹ Briefly, a spark discharge between Ti rods (Ti-452564, Nilaco, Japan) under air flow was employed to produce aerosol TiO₂ nanoparticles, and the particle laden flow was employed as the operating gas for atomizing the rGO solution (rGO in ethanol). The TiO₂ particles passed over the atomizer orifice, where they mixed with atomized rGO through a heated tubular reactor (GTF 12/25/364, Lenton Furnaces, UK) at 90 °C wall temperature to drive the solvent from the flow *via* mechanical filtration. P25-TiO₂@LrGO was prepared by simply mixing commercial p25-TiO₂ and LrGO

powders in ethanol under sonication. Low- and high-magnification TEM images (Fig. 4a) show the morphology of rGO, TiO₂@rGO, and p25-TiO₂@LrGO samples. The morphology of rGO resembled flakes, and the flake size was about 47 nm in lateral dimension with about 0.36 nm in the *d*-spacing (see the inset). When the TiO₂ particles passed over the orifice of the collision atomizer, most TiO₂ particles were deposited onto the rGO flakes, resulting in TiO₂@rGO hybrid nanocomposites. The morphology of p25-TiO₂@LrGO (also shown in Fig. 4a) reveals a dispersion in the LrGO matrix, which has a tendency to locate along the wrinkles and edges of the graphene sheets. The time profiles of hydrogen production are compared among samples in Fig. 4b. Compared with TiO₂@rGO, TiO₂@GO shows a lower performance for hydrogen production. The nanoscale rGO hybridized structure further assisted the photocatalysis by withdrawing electrons and subsequently retarding the charge pair recombination. Nevertheless, the present TiO₂@GO shows a comparable performance to p25-TiO₂@LrGO for hydrogen production, which might be ascribed to the morphological difference between p25-TiO₂@LrGO (only a small fraction of the TiO₂ surface is in direct contact with LrGO) and TiO₂@GO (significantly smaller TiO₂ particles on graphitic layers). This implies that the ambient plasma synthesis of TiO₂@GO composites did make an appropriate structure for the comparable photocatalytic performance without individual

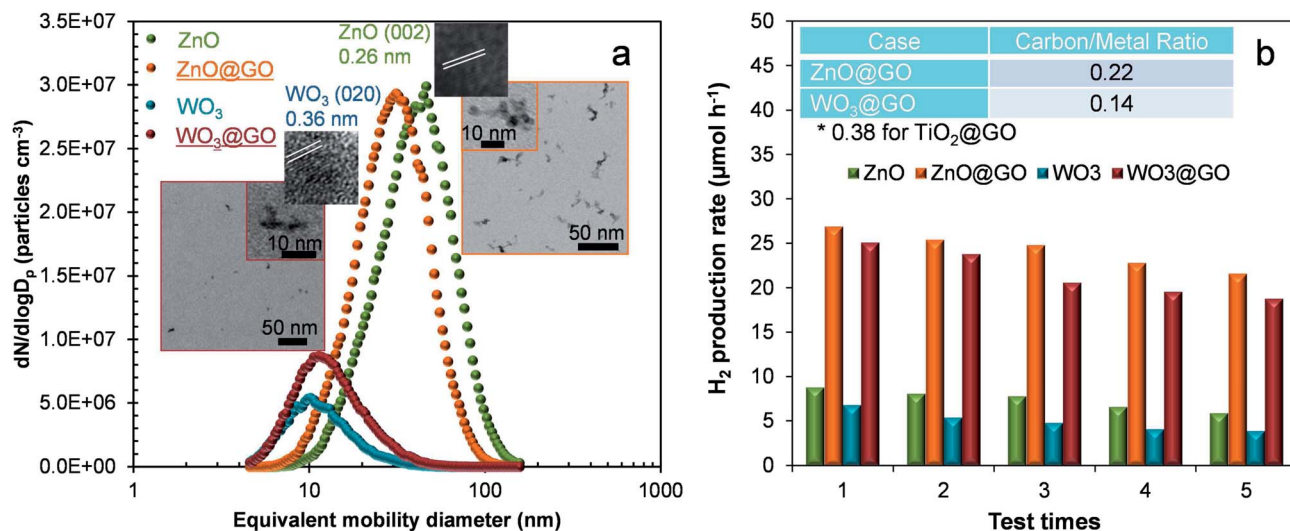


Fig. 5 Results of other heterogeneous spark configurations. (a) Size distributions of spark-produced ZnO and WO_3 nanoparticles, and their hybridized nanostructures with thin GO layers (ZnO@GO and $\text{WO}_3\text{@GO}$) in the gas-phase. Standard deviations are noted in Table S2.† Low- and high-magnification TEM images of ZnO@GO (27 ± 5.2 nm) and $\text{WO}_3\text{@GO}$ (11 ± 2.2 nm) nanocomposites are also shown as insets. (b) Time profiles of hydrogen production with ZnO@GO and $\text{WO}_3\text{@GO}$ nanocomposites. The atomic ratios between the carbon and metal of ZnO@GO and $\text{WO}_3\text{@GO}$ as well as $\text{TiO}_2\text{@GO}$ from energy dispersive X-ray measurements are also displayed.

preparation of rGO. After five cycles (Fig. 4c), we found that the hydrogen production performances of $\text{TiO}_2\text{@rGO}$ and p25- $\text{TiO}_2\text{@LrGO}$ were reduced by ca. 7% and 5%, suggesting that the rGO hybridization also has good stability and reusability. On the other hand, the slight decreases in the performance are also shown in rGO hybridization cases, which imply that the rGO hybridization did not show a significant better stability in repetitive use.

As a significant expansion of this work, Fig. 5 shows the size distributions, morphologies, and photocatalytic activities of other nanocomposites from different spark configurations (zinc-graphite and tungsten-graphite under identical operation conditions) to verify the generalizability of the heterogeneous spark discharge. As shown in Fig. 5a, even though the other nanocomposites display different intrinsic size distributions, due to different material combinations, the size distributions of the metallic nanoparticles converged toward the nanocomposite size distribution (refer to Fig. 1), and there was no bimodal distribution character. This implies that the heterogeneous spark discharge may induce an appropriate incorporation of GO with metallic nanoparticles. Details of the size distributions are summarized in Table S2.† Fig. 5a also shows that the morphologies of ZnO@GO and $\text{WO}_3\text{@GO}$ nanocomposites consisted of ZnO and WO_3 nanocrystals, although the spark electrodes for the synthesis were changed. There was only a difference in the morphology of the nanocomposites because of the different ratios between carbon and the metal (inset of Fig. 5b). This ambient plasma would be generalizable although the material changed. We further evaluated the photocatalytic activities of nanocomposites for hydrogen production and compared the results to those obtained from individual ZnO and WO_3 nanoparticles (Fig. 5b). Even though there were differences in the photocatalytic activity, both nanocomposites showed better performance than individual

metallic nanoparticles. Moreover, the performance differences between the nanocomposites ($\text{TiO}_2\text{@}$, ZnO@ , and $\text{WO}_3\text{@GO}$) may have originated from their intrinsic structures, but it is very difficult to synthesize nanocomposites having the same morphology, size, and crystalline structure for different material combinations. Therefore, we cannot simply discuss the performance differences in photocatalysis between the nanocomposites; nevertheless, one can conclude that the incorporation of metallic nanoparticles with GO layers in a nanoscale dimension has a synergetic effect accounting for the enhanced photocatalytic activities.

Conclusions

We developed for the first time a continuous gas-phase synthesis of $\text{TiO}_2\text{@GO}$ nanocomposites through an ambient heterogeneous spark discharge without any wet chemical preparation steps, and we also tested their photocatalytic activities. The unique hybrid structure enabled enhanced contact between GO and TiO_2 and facilitated efficient electron transfer for enhanced photocatalytic activities for hydrogen production. We believe that this provides new perspectives and useful information for the design of low-cost and more efficient photocatalysts for energy production and environmental remediation.

Notes and references

- 1 P. Zhang, C. Shao, Z. Zhang, M. Zhang, J. Mu, Z. Guo and Y. Liu, *Nanoscale*, 2011, 3, 2943.
- 2 Y. Wang, R. Shi, J. Lin and Y. Zhu, *Energy Environ. Sci.*, 2011, 4, 2922.
- 3 L. Chen, F. Chen, Y. Shi and J. Zhang, *J. Phys. Chem. C*, 2012, 116, 8579.

- 4 J. Zhong, F. Chen and J. Zhang, *J. Phys. Chem. C*, 2010, **114**, 933.
- 5 Y. Park, S.-H. Kang and W. Choi, *Phys. Chem. Chem. Phys.*, 2011, **13**, 9425.
- 6 M. Haro, L. F. Velasco and C. O. Ania, *Catal. Sci. Technol.*, 2012, **2**, 2264.
- 7 L. Zhang, H. Cheng, R. Zong and Y. Zhu, *J. Phys. Chem. C*, 2009, **113**, 2368.
- 8 M. Wojtoniszak, D. Dolat, A. Morawski and E. Mijowska, *Nanoscale Res. Lett.*, 2012, **7**, 235.
- 9 Q. Xiang, J. Yu and M. Jaroniec, *Nanoscale*, 2011, **3**, 3670.
- 10 Q. Xiang, J. Yu and M. Jaroniec, *J. Am. Chem. Soc.*, 2012, **134**, 6575.
- 11 G. Lui, J.-Y. Liao, A. Duan, Z. Zhang, M. Fowler and A. Yu, *J. Mater. Chem. A*, 2013, **1**, 12255.
- 12 Y. Dai, Y. Sun, J. Yao, D. Ling, Y. Wang, H. Long, X. Wang, B. Lin, T. H. Zeng and Y. Sun, *J. Mater. Chem. A*, 2014, **2**, 1060.
- 13 Q. Xiang, J. Yu and M. Jaroniec, *Chem. Soc. Rev.*, 2012, **41**, 782.
- 14 J. H. Byeon and Y.-W. Kim, *ACS Appl. Mater. Interfaces*, 2013, **5**, 3959.
- 15 J. H. Byeon and Y.-W. Kim, *Chem. Eng. J.*, 2013, **229**, 540.
- 16 R. Leary and A. Westwood, *Carbon*, 2011, **49**, 741.
- 17 L.-W. Zhang, H.-B. Fu and Y.-F. Zhu, *Adv. Funct. Mater.*, 2008, **18**, 2180.
- 18 T. Jiang, Z. Tao, M. Ji, Q. Zhao, X. Fu and H. Yin, *Catal. Commun.*, 2012, **28**, 47.
- 19 P. Zeng, Q. Zhang, X. Zhang and T. Peng, *J. Alloys Compd.*, 2012, **516**, 85.
- 20 S. Mayavan, J.-B. Sim and S.-M. Choi, *J. Mater. Chem.*, 2012, **22**, 6953.
- 21 J. H. Byeon and J.-W. Kim, *Appl. Phys. Lett.*, 2010, **96**, 153102.
- 22 J. H. Byeon, J. H. Park and J. Hwang, *J. Aerosol Sci.*, 2008, **39**, 888.
- 23 T.-F. Yeh, J.-M. Syu, C. Cheng, T.-H. Chang and H. S. Teng, *Adv. Funct. Mater.*, 2010, **20**, 2255.
- 24 J. H. Byeon and J. T. Roberts, *ACS Appl. Mater. Interfaces*, 2012, **4**, 2693.